Applied Catalysis B: Environment and Energy 371 (2025) 125203

Contents lists available at ScienceDirect

Applied Catalysis B: Environment and Energy

journal homepage: www.elsevier.com/locate/apcatb

Stable dual metal oxide matrix for tuning selectivity in acidic electrochemical carbon dioxide reduction

Ziling Zhang [a], Thành Trần-Phú [b,*], Jodie Yuwono [c,*], Zhipeng Ma [d], Yuwei Yang [d], Josh Leverett [d], Rosalie K. Hocking [b], Bernt Johannessen [e], Priyank Kumar [d], Rose Amal [d,*], Rahman Daiyan [a,*]

[a] School of Minerals and Energy Resources Engineering, The University of New South Wales Sydney, Sydney, NSW 2052, Australia
[b] School of Science, Computing and Engineering Technologies, Swinburne University of Technology, Hawthorn, VIC 3122, Australia
[c] School of Chemical Engineering, The University of Adelaide, Adelaide, South Australia 5005 Australia
[d] School of Chemical Engineering, The University of New South Wales Sydney, Sydney, NSW 2052, Australia
[e] Australia's Nuclear Science and Technology Organisation, 800 Blackburn Road, Clayton, VIC 3168, Australia

ARTICLE INFO

Keywords:
CO_2 reduction
Electrocatalysis
Acid stable
In situ XAS

ABSTRACT

The acidic electrochemical CO_2 reduction reaction (CO_2RR) holds promise for achieving a carbon-neutral future and can promote efficient CO_2 utilization by attenuating the carbonate/bicarbonate formation reaction. However, catalyst degradation in strong acids and the competing hydrogen evolution reaction (HER) often result in short catalyst lifetime and poor product selectivity. Herein, this study introduces a strategy to stabilize copper oxide (CuO_x) catalysts for acidic CO_2 reduction (CO_2RR) by incorporating bismuth oxide (BiO_x) and achieved a maximum formic acid Faradaic efficiency (FE_{HCOOH}) of 97 ± 1 % at −2.7 V *vs.* RHE and maintaining over 90 % FE for more than 20 h. *In situ* XAS, SR-FTIR and density functional theory (DFT) calculations show that the catalyst can inhibit *H adsorption and promote selective CO_2 conversion to HCOOH via the HCOO* pathway. Further electrolyte anion modulation achieves ethanol and acetone production at Faradaic efficiencies of 17 % and 16 % in phosphoric and perchloric acid, respectively. *In situ* analyses reveal that distinct anion adsorption influence key intermediates, such as *CO, leading to shifts in C_{2+} product distributions. This work offers insights into designing acid-stable electrocatalysts for CO_2RR and highlights the potential of electrolyte modification to tailor product selectivity.

1. Introduction

Electrochemical carbon dioxide reduction reaction (CO_2RR) is considered a promising pathway to close the carbon cycle and to generate synthetic chemicals and fuels, powered by renewable energy sources [1–3]. Currently, most CO_2 reduction studies are conducted in alkaline or near-neutral electrolytes, as alkaline environments have been demonstrated to yield optimal cathode performance for products such as methane [4,5], and to promote carbon–carbon coupling reactions necessary for generating C_{2+} products [6,7], while also suppressing the competing hydrogen evolution reaction (HER) [8–11]. However, the side reaction between CO_2 and OH^- causes undesired CO_2 consumption and crossover, lowering carbon utilization and energy efficiencies [12–15]. Furthermore, the resultant accumulation of the generated carbonate and byproducts is reported to significantly lower the catalyst stability and cell durability [16–18]. Among the emerging strategies, acidic CO_2RR offers a viable approach since hydronium ions (H_3O^+) are present as proton source, and limited hydroxide ions (OH^-) are generated during electrolysis to produce parasitic carbonate ions [19,20]. In addition, acidic electrolysis can outperforms its alkaline counterpart by exhibiting lower ohmic resistance and higher current density (*j*), attributed to the superior conductivity of H_3O^+ (350 S cm^2 mol^{-1}) over OH^- (198 S cm^2 mol^{-1}) [21,22]. However, limiting the competing hydrogen evolution reaction (HER) is a challenge under acidic environment, owing to presence of excess protons, and the harsh environment shortens catalyst lifespan, hampering its practical deployment.

Copper (Cu) and oxide-derived Cu catalysts have been reported to be highly effective in acidic CO_2RR, owing to the presence of active Cu^*

* Corresponding authors.
E-mail addresses: thanhtran@swin.edu.au (T. Trần-Phú), jodie.yuwono@adelaide.edu.au (J. Yuwono), r.amal@unsw.edu.au (R. Amal), r.daiyan@unsw.edu.au (R. Daiyan).

https://doi.org/10.1016/j.apcatb.2025.125203
Received 19 November 2024; Received in revised form 21 February 2025; Accepted 21 February 2025
Available online 26 February 2025

species and defect sites that enhance CO_2 adsorption and activation [23–25]. These catalysts can facilitate the conversion of CO_2 into a wide range of products, from CO, formic acid to C_{2+} products [26]. For instance, Li et al. showed that graphene oxide wrapped Cu nanowires demonstrated a Faradaic efficiency (FE) of 55 % for CO_2 to CH_4 [27]. Cao et al. developed an electro-deposited Cu catalyst that achieved a 60 % FE for ethylene in 0.05 M sulfuric acid electrolyte [28]. However, the catalyst stability is generally poor under such reaction conditions with less than 10 h of reported data. It is therefore imperative to develop acid-stable Cu based CO_2RR catalysts for reaping benefits associated with acidic electrolysis that is also capable of tuning product selectivity.

Several strategies have been developed for acidic water electrolysis, including the structure modification and surface engineering of acid-stable precious metals and their oxides [29–33]. Surface coating or wrapping the electrocatalyst with anticorrosive adlayers is another way widely used to enhance catalyst stability [34–37]. However, these strategies are not directly applicable to CO_2RR as the introduction of noble metals or passivation layers can significantly alter the active sites of the catalyst and further promote HER [38], and the adlayers and core/shell structure can limit conductivity and mass transport within the catalyst diffusion layer [39,40]. Current research on acidic CO_2RR excessively focuses on the HER suppression through augmenting the hydrophobicity of the microenvironment [40,41], modulating electronic structure by metal alloying [42–44], and morphology control [45,46]. While these approaches have shown improved performance, the dual strategy of HER suppression and stability enhancement especially for the non-precious metal-derived electrocatalysts with facile synthesis method warrants further investigation.

Herein, we propose the use of *p*-block metal oxides, such as BiO_x within CuO_x matrix as a strategy to stabilize the catalyst in acidic environment. Pourbaix diagram indicates the robust stability of *p*-block oxides in acidic solution, and these materials have been successfully applied to the anodic oxygen evolution reaction (OER) in acid [47–49]. The *in situ* synchrotron based X-ray absorption spectroscopy (XAS) measurements confirmed the efficacy of our approach. The *in situ* Fourier transform infrared transmission (FTIR), and density functional theory (DFT) reveal that the combination of BiO_x and CuO_x suppress *H adsorption and increases the energy difference between two reaction pathways, synergistically enhancing the selective CO_2RR-HCOOH performance. Building on this stable dual metal oxide matrix, we also explore the role of anions in controlling product selectivity during acidic CO_2RR. By varying the electrolyte from SO_4^{2-} to PO_4^{3-} or ClO_4^-, we observe shifts in product selectivity from formic acid to ethanol (with a Faradaic efficiency of 17 % at −1.7 V *vs.* RHE) and then to acetone (16 % at −2.2 V *vs.* RHE). Our characterization techniques show that anions exhibit distinct adsorption behaviors, altering the bounded key intermediates and influencing the distribution of C_{2+} products.

2. Experimental section

2.1. Catalyst preparation

The catalysts were synthesized employing a custom-built flame spray pyrolysis (FSP) apparatus, as described in our previous works [50–53]. The bi-metallic Cu/Bi precursor was prepared through the combination of copper(II) naphthenate in mineral spirits (8 % Cu, Strem Chemicals) and bismuth(III) 2-ethylhexanoate (70–75 % in xylenes, 24 % Bi, Strem Chemicals). The precursors were dissolved in a 1:1 (vol) mixture of toluene (anhydrous 99.8 %, Sigma-Aldrich) and 2-ethylhexanoic acid (99 %, Sigma-Aldrich), constituting a total metal precursor with concentration of 0.2 M. The resultant precursor solution was injected into the FSP system through a syringe pump at a volume flow of 5 mL min^{-1} and atomized with an oxygen flow of 5 mL min^{-1} (Coregas, 99.9 %). The flame was ignited and maintained using supporting gas, which has a composition of 3.2 L min^{-1} oxygen and 1.5 L min^{-1} methane (Coregas, 99.95 %). After the flame synthesis and filtration, the collected catalyst powder was used for characterization and for fabricating working electrodes to be tested in the flow electrolyzer. The CuO_x and BiO_x catalysts were synthesized following the same procedure with only copper(II) naphthenate or bismuth(III) 2-ethylhexanoate as the precursor.

2.2. Electrochemical measurements

The CO_2RR performance of the as-prepared catalysts was tested in a three-electrode flow cell, Ag/AgCl electrode stored in saturated KCl (Gauss Union) was used as the reference electrode in the catholyte chamber, and commercial Iridium oxide/ionomer mixture coated on carbon paper (Dioxide MaterialsTM) was used as the counter electrode. The pretreated Nafion 117 membrane (Gauss Union) was used as the proton exchange membrane to separate the cathode and anode compartments. Electrochemical measurements were conducted using an Autolab M204 and Booster 10 A (Metrohm Autolab) electrochemical workstation.

2.3. In situ material characterization

The *in situ* XAS spectra were recorded at the Australian Synchrotron ANSTO, operating at 3.0 GeV with a current of 500 mA, at the Copper K-edge and Bismuth L_3-edge. Data were acquired in fluorescence mode using three N_2-filled ionization chambers in series as detectors. Spectra were acquired under room temperature, using an in-house designed cell. Energy calibration was achieved by simultaneously recording the spectrum of copper foil, for which the energy of the first maximum in the first derivative is 8980 eV [54]. XAS data were processed and analyzed using the Demeter software package [55].

The *in situ* SR-FTIR measurements were carried out at the Australian Synchrotron ANSTO using SR-FTIR setup equipped with a ZnSe crystal as the infrared transmission window (cut-off energy 625 cm^{-1}) and a specific designed FTIR cell. An infrared microscope (Bruker Hyperion 3000 with an x20 objective) was coupled with an FTIR spectrometer (Bruker 70 v s^{-1}) equipped with a KBr beam splitter and liquid-nitrogen-cooled mercury cadmium telluride detector. The cell was connected to an electrochemical workstation (Metrohm Autolab M204) to supply voltage. Before each systematic measurement, the background spectrum of the catalyst electrode was acquired at open-circuit potential, with the cell filled with electrolyte and measured without any applied potential. The infrared absorption spectrum was acquired by averaging 256 scans at a resolution of 2 cm^{-1}.

The detailed methods for electrochemical measurements, product quantification, material characterization and DFT calculations are available in Supplementary information.

3. Results and discussion

3.1. Stability enhancement of CuO_x/BiO_x in acidic environment

The CuO_x/BiO_x catalysts were synthesized using our previously reported facile and scalable one-step flame spray pyrolysis (FSP) synthesis approach [51–53,56]. The transmission electron microscopy (TEM) images (Fig. S1-S3) prove the co-existence of CuO and Bi_2O_3 for the as-synthesized catalyst, with lattice spacing of 2.31 Å and 3.18 Å, corresponding to the (111) facet of CuO and the (201) facet of Bi_2O_3, respectively. These observations are consistent with the XRD patterns (Fig. S4). Physiochemical characterizations verify the formation of CuO_x/BiO_x dual metal oxides, and energy dispersive X-ray spectroscopy (EDS) elemental mapping indicates the uniform distribution of Cu, Bi, and O elements on the carbon substrate (Fig. S5). XPS analysis also confirmed the surface atomic composition and valence state of the CuO_x/BiO_x catalyst (Fig. S6). Both EDS and XPS indicate a Cu/Bi composition ratio of approximately 1:1, aligning well with the intended stoichiometry in our synthesis, confirming that the targeted composition

was successfully achieved.

When tested for CO_2RR, the CuO_x/BiO_x catalyst demonstrates significantly improved stability compared to the as-prepared CuO_x catalyst within a flow cell electrolyzer (Fig. 1a). At −2.3 V *vs.* RHE, the *j* for the CuO_x catalyst declines from −65 mA cm^{-2} to −35 mA cm^{-2} during the first 4 h, indicating a loss of catalyst activity. In sharp contrast, the *j* for CuO_x/BiO_x catalyst remains stable for over 10 h at approximately −70 mA cm^{-2}. Similarly, at −2.7 V *vs.* RHE (the potential corresponding to the highest Faradaic efficiency for CuO_x/BiO_x catalyst), the *j* of the CuO_x catalyst decreases from −95 mA cm^{-2} to −80 mA cm^{-2} within the first 4 h. After 5 h, flooding of the electrode was observed, with an increase in FE_{H2} from 24 % in the first hour to over 40 % while the CuO_x/BiO_x catalyst remains stable for over 10 h, maintaining a *j* of approximately −105 mA cm^{-2} (Fig. S7). This difference can be attributed to CuO dissolution in acidic media, which alters the electrode morphology, and CuO reduction under cathodic conditions, leading to changes in active sites [57,58]. The *ex situ* XRD analysis of the CuO_x electrode before and after the reaction reveals that the characteristic peaks of CuO disappear, while a new peak at 37° corresponding to Cu_2O (111) emerges (Fig. S8), confirming the partial reduction of CuO [59,60]. The CO_2RR stability test conducted in the H-cell for the CuO_x catalyst exhibits a similar degradation trend (Fig. S9), where the current density declines during the first few hours and fluctuates over the first 10 h.

The X-ray absorption near edge structure (XANES) spectra, collected on Cu K-edge using Cu, Cu_2O, and CuO as references, and on Bi L_3-edge using Bi_2O_3 as reference, were used to investigate the valence state and coordination environment of the Cu and Bi species on the CuO_x/BiO_x catalyst. The XANES spectrum of Cu K-edge for CuO_x/BiO_x overlapped with that of the CuO reference and that of Bi L_3-edge overlapped with the Bi_2O_3 reference (Fig. S10-S11). It indicates that the Cu and Bi elements appeared as Cu^{2+} and Bi^{3+} in the catalyst, in good agreement with the previous TEM, XRD, and XPS results. The Fourier transformed extended X-ray absorption fine structure (FT-EXAFS) at the Cu K-edge of the catalyst exhibited the peak at around 1.53 Å, which is consistent with Cu-O species, the lack of Cu-Cu scattering path also suggests that the Cu species in the CuO_x/BiO_x are fully oxide (Fig. 1b). Similarly, the FT-EXAFS at the Bi L_3-edge revealed that the catalyst exhibited a coordination structure similar to that of the Bi_2O_3 reference (Fig. 1c), without a distinctive Bi-Bi scattering path characteristic of Bi foil, which typically appears at approximately 3 Å, as reported in the literature [61,62]. Taken together with other characterization techniques, our results provide strong evidence of the formation of well-dispersed CuO_x/BiO_x dual metallic oxide without the formation of solid solutions and bimetallic compounds.

The *in situ* XAS spectrum collected at different potentials during the CO_2RR in sulfuric acid (pH 2, cation concentration $[K^+] = 0.5$ M) are shown in Fig. 2, with the reference spectra of metallic Cu foil, Cu_2O, CuO, and Bi_2O_3 plotted. The Cu K-edge spectra show a shift toward lower energy (Fig. 2a) at an applied potential of −0.6 V *vs.* RHE. Under more negative potentials, we note that the absorption threshold passed that of Cu_2O and continued moving toward the position of Cu foil reference. A decrease in the white-line intensity during the reaction with more negative applied potentials was also observed, suggesting that the Cu oxidation state was decreasing during the reaction at −1.0 V *vs.* RHE, aside from the decrease in white-line intensity, the feature above the edge also gradually changed towards a two-peak feature characteristic of metallic Cu [63]. This trend is also clearly presented by EXAFS (Fig. S12a), the *ex situ* EXAFS patterns are similar to the CuO reference while the pathway changes with applied potential.

FT-EXAFS of Cu K-edge (Fig. 2c) reveals a decline in the intensity of the Cu-O bond at 1.6 Å and an increase in the Cu-Cu scattering peak at 2.3 Å compared to the measurements obtained at OCP, that could be attributed to a partial transformation from CuO to metallic Cu^0, which is consistent with the findings in XANES spectra. Similarly, from the Bi L_3-edge XANES spectra, a shift toward lower energy and a decrease in white-line intensity suggests the reduction of Bi^{3+} towards lower oxidation states (Fig. 2b). The FT-EXAFS spectrum shows a decline in Bi-O scattering peak (1.56 Å) intensity at −0.6 V *vs.* RHE, followed by an increase with more negative applied potentials [64]. The initial decline in the Bi–O scattering peak suggests the onset of partial reduction of BiO_x, likely due to the removal of some oxygen from the Bi coordination sphere. As the potential becomes more negative, a restructuring of the BiO_x phase occurs, possibly through a dynamic equilibrium between reduction and re-oxidation, resulting in a restored or even enhanced Bi–O coordination rather than complete reduction to metallic Bi. The Bi-Bi scattering path at about 3.09 Å is also observed at −1.0 V *vs.* RHE, indicating the existence of metallic Bi under higher redox potential (Fig. 2d) [61,65]. The comparison of EXAFS spectra at Cu K-edge and Bi L_3-edge of the CuO_x/BiO_x catalyst shows distinct difference from each other, it is therefore, unlikely that BiO_x is doped into CuO_x, but presents as a separate phase and intimately intermixed with CuO_x to produce a nanocomposite (Fig. S12) [66]. It is also confirmed by the XRD patter of the CuO_x/BiO_x catalyst before and after the reaction, the results indicate that no detectable Cu_xBi_y phase formed during electrolysis, as no additional peaks corresponding to such an alloy were observed (Fig. S13). The Pourbaix diagrams further supports the robustness of BiO_x in acidic solutions, suggesting that its presence is key to the enhanced stability of the catalyst compared to the CuO counterpart [67].

3.2. *Electrochemical CO_2RR performance*

Equipped with the above findings, we then tested the dual metal oxide matrix catalyst for acidic CO_2RR in H_2SO_4 electrolyte (pH 2) in a flow cell electrolyzer (Fig. S14), revealing higher *j* compared to constituent CuO_x and BiO_x catalysts, respectively. Specifically, the $CuO_x/$

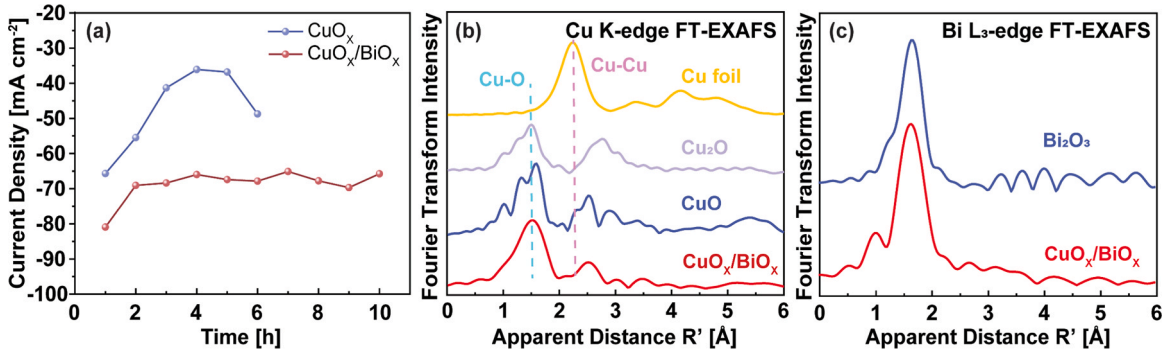

Fig. 1. (a) Stability comparison of CuO_x and CuO_x/BiO_x conducted in sulfuric acid (pH 2) in the flow cell electrolyzer at −2.3 V *vs.* RHE. (b-c) The *ex situ* Cu K-edge FT-EXAFS spectra of CuO_x/BiO_x catalyst with Cu foil, Cu_2O, and CuO as references. (c) The *ex situ* Bi L_3-edge FT-EXAFS spectra of CuO_x/BiO_x catalyst with Bi_2O_3 as the reference.

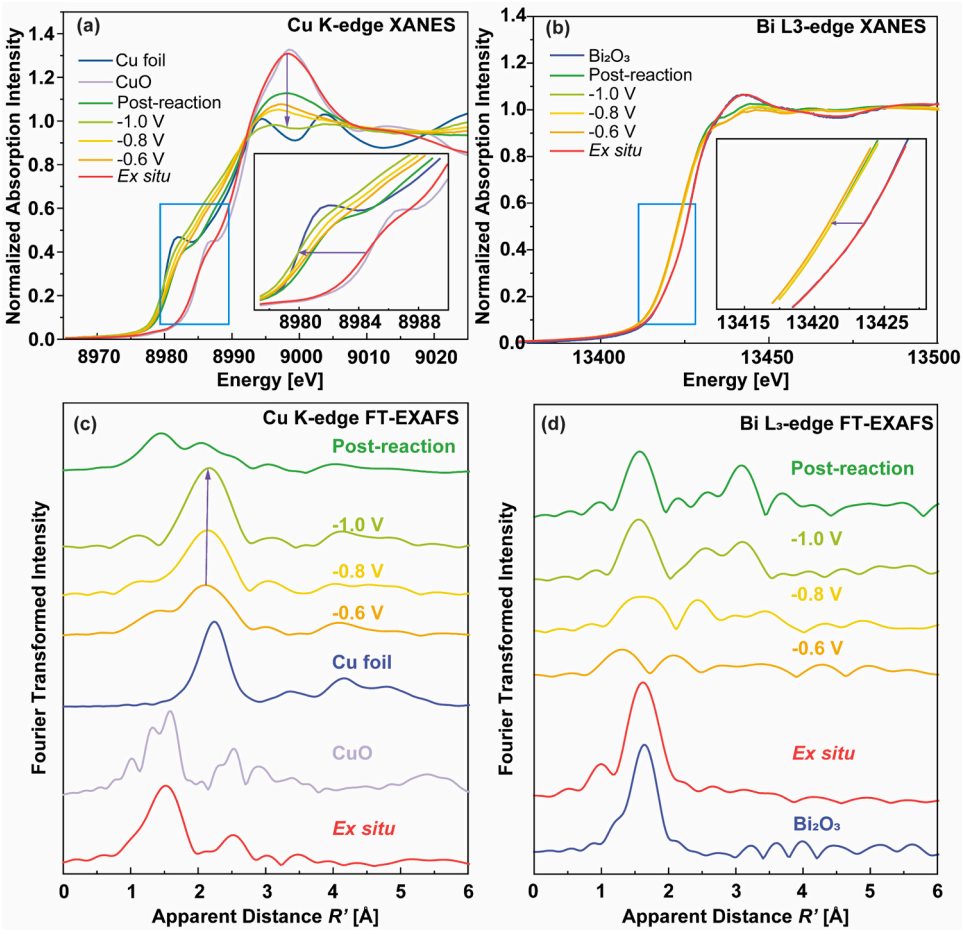

Fig. 2. *In situ* XAS results for CuO_x/BiO_x catalyst in sulfuric acid (pH 2, additional cation $[K^+]$ = 0.5 M) at different applied potentials. (a) Normalized Cu K-edge XANES. (b) Normalized Bi L_3-edge XANES. (c) FT-EXAFS of Cu K-edge. (d). FT-EXAFS of Bi L_3-edge. FT-EXAFS (dash lines) of CuO, Cu_2O, Cu foil and Bi_2O_3 references are presented in panel c and d to assist the comparison.

BiO_x display a *j* of −189 mA cm^{-2} at −3.7 V *vs.* RHE whereas CuO_x and BiO_x display only −152 mA cm^{-2} and −154 mA cm^{-2} at the same applied potential, respectively (Fig. 3a).

The enhanced performance of the CuO_x/BiO_x catalyst was also demonstrated by its high FE towards formic acid (Fig. 3b), which was maintained > 93 % across a wide potential range from −1.7 to −3.7 V *vs.* RHE, with negligible formation of H_2 and CO (<5 %). Notably, the catalyst achieved a maximum FE_{HCOOH} of 97 ± 1 % at −2.7 V *vs.* RHE. Owing to the relatively high cell resistance of the flow cell system, IR compensated applied potential is about −1.4 V *vs.* RHE. The performance is comparable with the Bi-based catalysts reported in the literature [62,68,69]. In comparison, BiO_x displayed a FE_{HCOOH} > 95 % at −1.7 V *vs.* RHE, which is consistent with the unfavorable *COOH intermediates adsorption towards CO production, generally presented by Bi-based catalysts [70]. The high selectivity towards formic acid of CuO_x/BiO_x and BiO_x at low overpotential can be attributed to the intrinsic inertness of Bi toward HER [71,72], where the activation of HER requires higher potential compare to CO_2RR on Bi catalysts [73,74]. However, the formic acid selectivity declines significantly (FE < 60 % at −2.7 V *vs.* RHE) for BiO_x at more negative potential when the competing HER takes place at more negative overpotentials. This is likely because the intimate mixing of CuO_x and BiO_x modulates the local electronic environment, lowering the energy barrier for HCOO* formation and suppressing competing reaction pathways (e.g., *COOH formation), as supported by DFT calculations. Moreover, under strong cathodic polarization, a dynamic equilibrium between reduction and re-oxidation helps stabilize the active sites, thereby sustaining high formic acid selectivity even at −2.7 V *vs.* RHE. In contrast, CuO_x catalyst obtained FE_{HCOOH} of around 55 % at low potentials of −1.7 V *vs.* RHE and producing a mixture of C_1 and C_2 products across the potential range tested, consistent with reported CuO catalysts [75]. When comparing production rate, we note that yield for CuO_x/BiO_x is 803 nmol s^{-1} cm^{-2} at −3.7 V *vs.* RHE compared to BiO_x and CuO_x yield rate of 174 nmol s^{-1} cm^{-2} and 78.7 nmol s^{-1} cm^{-2}, higher than the catalyst reported in literature under similar *j* (Fig. 3c and Table S3) [76]. The stability of this catalyst was further confirmed where *j* remained at around −100 mA cm^{-2} at −2.7 V *vs.* RHE with FE_{HCOOH} stabilized > 90 % for 20 h of operation (Fig. 3d). The synthesized CuO_x/BiO_x demonstrates outstanding HER suppression capability and enhanced product selectivity at more negative potentials compared with the single metal oxide counterparts. As a result, it is important to study the structure of evolution and underlying mechanisms to unveil such improvements.

To investigate coordination numbers, binding distances, and Debye–Waller parameters, we performed a simplified three-parameter fit of the FT-EXAFS data acquired between −0.6 and −1.0 V *vs.* RHE. Although the Cu K-edge XANES indicates partial reduction of CuO_x, it is not fully converted to metallic Cu within the *in situ* measurement duration, as evidenced by a slightly higher white line intensity relative to the Cu foil reference. Our fitting results reveal that the coordination number (CN) of Cu–O decreases with increasing cathodic potential, while the CN of Cu–Cu correspondingly increases from 1.65 to 9.52. Similarly, the CN for all three Bi–O scatterings decrease from 1.80 to 0.51, and a metallic Bi–Bi scattering path emerges at −1.0 V *vs.* RHE, indicating that both Cu^{2+} and Bi^{3+} sites undergo changes in their

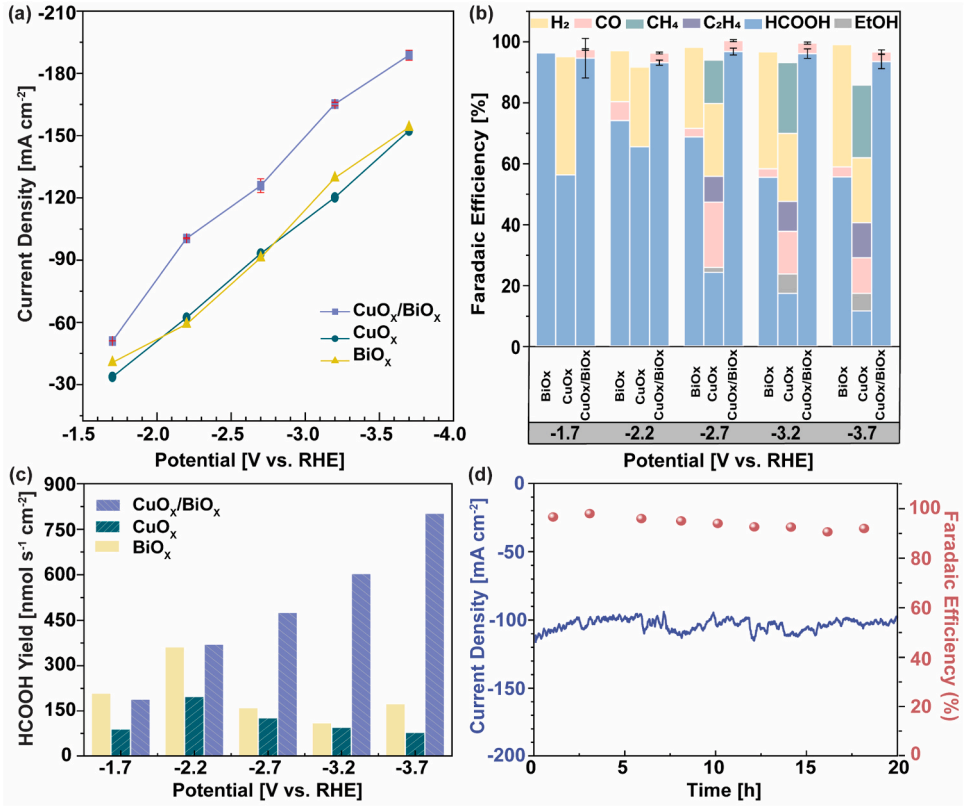

Fig. 3. CO_2RR of CuO_x/BiO_x, CuO_x, and BiO_x. (a) Current density under different applied potentials. (b) Faradaic efficiency of catalysts in sulfuric acid (pH 2, additional cation $[K^+] = 0.5$ M) under different applied potentials. (c) Formic acid yield. (d) Stability tests of CuO_x/BiO_x at −2.7 V *vs.* RHE.

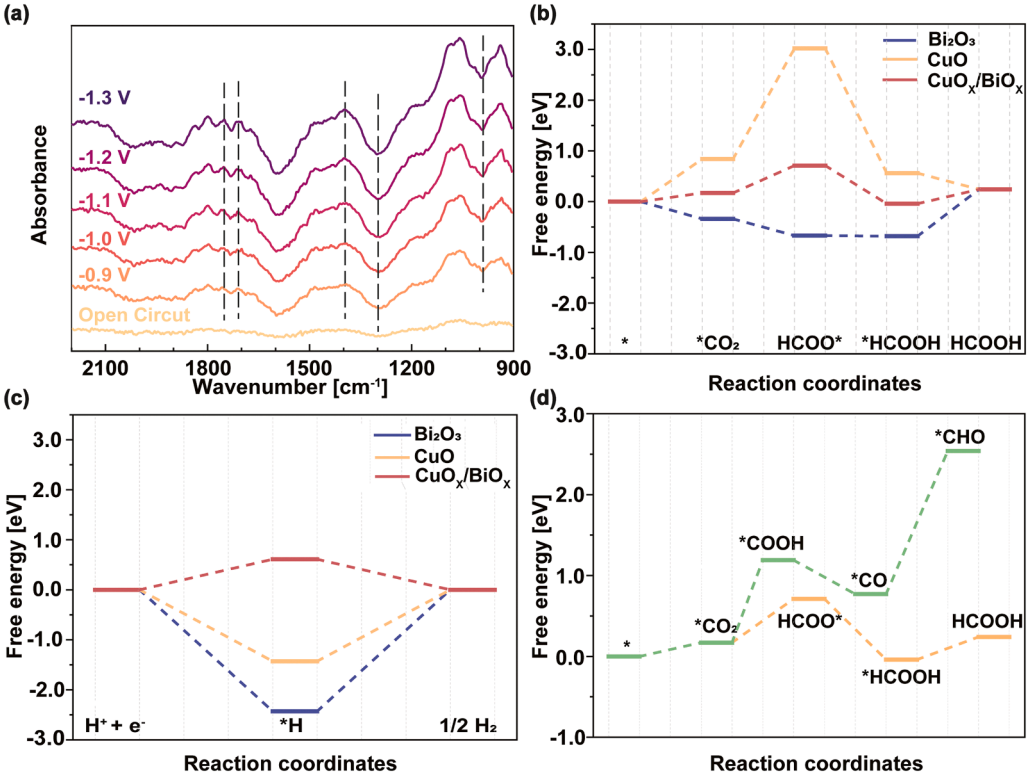

Fig. 4. Mechanism study. (a) *In situ* SR-FTIR of CuO_x/BiO_x sample. The dash lines shown refer to the peak locations of key species. (b-d) Free energy calculation for (b) CuO_x/BiO_x, CuO, and Bi_2O_3 catalysts towards HCOOH production, (c) CuO_x/BiO_x, CuO, and Bi_2O_3 catalysts towards H_2 production, and(d) CuO_x/BiO_x towards HCOOH and *CHO.

coordination environments and are partially reduced to Cu^{+}/Cu^{0} and Bi^{0}, respectively (Fig. S16, S17; Tables S1, S2).

Due to the challenges of acquiring reliable *in situ* XAS data at more negative potentials, we supplemented our analysis with *ex situ* XPS (Fig. S15) and XRD (Fig. S13) measurements before and after reaction. The post-reaction XRD patterns reveal that CuO is partially reduced to metallic Cu, while characteristic peaks corresponding to Cu_2O persist, indicating that under high overpotentials the catalyst comprises a composite of reduced Cu^{+} or Cu^{0} indicating that under high overpotentials the catalyst comprises a composite of reduced Cu species (Cu^{+}/Cu^{0}) and residual copper oxide. Although post-reaction XPS indicates the exclusive presence of Bi^{3+} species [51,77], our *in situ* XAS results reveal partial reduction of Bi species to Bi^{0} already, as less negative applied potential, and the lack of characteristic signals could be due to the re-oxidation of Bi metal. Therefore, our combined *in situ* and *ex situ* analyses, confirm that the CuO_x/BiO_x catalyst undergoes partial reduction during CO_2RR, resulting in a dynamic composite that preserves synergistic interactions between Cu and Bi. This dynamic behavior is critical for stabilizing the active sites responsible for the selective production of formic acid under acidic conditions.

3.3. Mechanism study

In situ synchrotron radiation – Fourier transform infrared transmission (SR-FTIR) spectrum was collected at different applied potentials in CO_2-saturated pH 2, cation $[K^{+}] = 0.5$ M H_2SO_4 electrolyte using a custom-built FTIR cell (Fig. S18). As shown in Fig. 4a, we note a peak at 1395 cm^{-1}, ascribed to the vibration of rate determining formic acid species (HCOO*) [78], while peaks at 1716 cm^{-1} and 1751 cm^{-1} are assigned to the C═O stretch of formic acid monomer and dimer, respectively [79]. The peak intensity increases along with the production of formic acid [80]. We also note a declining intensity of peak at wavenumber of 1300 cm^{-1}, corresponding to the adsorbed HCO_3^{-} group, which is consumed during the reaction [80,81]. No obvious feature can be found in the region of 1900–2100 cm^{-1} that is associated with *CO formation, indicating that CO formation is inhibited at the catalyst surface, which is consistent with the selectivity results reported above. The peaks below 1100 cm^{-1} corresponds to the adsorption of sulfate species in the electrolyte, as also witnessed in spectra collected in Ar-saturated electrolyte (Fig. S19) [82]. From the *in situ* FTIR, we conclude that the reaction pathway for formic acid production of the CuO_x/BiO_x catalyst is through formation of the intermediate that binds to the catalyst surface through oxygen atom [83,84].

The *in situ* XAS spectra shows evidence on the role of Cu^{+}/Cu^{0} and Bi^{3+} during the CO_2 reduction process and the *in situ* SR-FTIR measurements further identify the HCOO* as the key intermediate towards formic acid production. Based on these findings, we carried out the density functional theory (DFT) calculations for both CuO_x, BiO_x, and CuO_x/BiO_x to probe the individual role of these single metal oxides within the CuO_x/BiO_x nanocomposite and unravel the underlying reason for enhanced activity and selectivity of CO_2RR.

The DFT results show that the required free energy change (ΔG) for CuO_x/BiO_x from $*CO_2$ to HCOO* is 0.54 eV, significantly lower than that of CuO (2.18 eV) (Fig. 4b). Moreover, a 0.28 eV energy barrier toward HCOOH on CuO_x/BiO_x, smaller than that of Bi_2O_3 (0.92 eV), suggesting a more favorable *HCOOH desorption from the catalyst surface. This synergistic interaction between Bi_2O_3 and CuO facilitates both HCOO* formation and product desorption, contributing to a more efficient overall electrocatalytic process. In addition, the ΔG of *H is 0.61 eV for CuO_x/BiO_x, larger than any of the ΔG required in the HCOOH pathway (0.17 eV for *CO2, 0.54 eV for HCOO*, and 0.28 eV for HCOOH), as shown in Fig. 4c. We further calculated the free energy towards *CHO and found that both Cu^{+} and Cu^{0} exhibit very similar free energy between the formation of *COOH and HCOO* (Fig. S19), which supports the notion that CuO can generate a mixture of products during CO_2RR. Notably, upon the addition of BiO_x, the catalyst demonstrates a distinct divergence in free energy profiles. For the CuO_x/BiO_x catalyst, the *COOH becomes unfavorable with a positive energy of 1.19 eV, while the HCOO* formation pathway remains more favorable at 0.71 eV (Fig. 4d). These results demonstrate that the outstanding FE_{HCOOH} of CuO_x/BiO_x are contributed by the energetically preferred pathway of HCOOH compared with other reaction pathways, thus leading to the single-distributed, superior CO_2RR performance towards formic acid, compared to its single metal oxide counterpart.

3.4. Electrolyte anion effect

We conducted CO_2RR using different electrolytes, including phosphoric acid and perchloric acid to gain a deeper understanding of the reaction mechanism, investigate the influence of the reaction environment and tune product selectivity. Our findings show that varying the anions in the electrolyte can tune product selectivity toward higher-value products (C_{2+}). Fig. 5a illustrates that the CuO_x/BiO_x catalyst in a pH = 3, $[K^{+}] = 1.1$ M phosphoric acid buffer achieved an FE_{EtOH} of 16.8 % at −1.7 V vs RHE but showed decreased HER suppression ability, with an FE_{H2} of above 40 % across all applied potentials. Compared to other electrolytes under the same pH, the catalyst exhibited poor HER suppression in a PO_4^{3-}-containing electrolyte at both pH 2 and pH 3 (Fig. 5b). This could be attributed to a pH gradient at the catalyst surface, as the phosphoric acid buffer is more effective at regulating the local pH at the catalyst surface, maintaining it closer to the bulk pH by producing H_3O^{+} ions, leading to a high concentration of protons at the catalyst surface and promoting HER [85,86]. Conversely, in a sulfate-containing electrolyte, after protons reach their diffusion limit near the catalyst surface, reduced CO_2 reacts with water to produce OH^{-}, which diffuses away from the electrode surfaces and reacts with protons before they reach the catalyst, thus suppressing HER [87]. Similar product selectivity changes were observed in ClO_4^{-} electrolytes, where acetone was produced with a Faradaic efficiency of 16.4 % at −2.2 V *vs.* RHE (Fig. 5b)

Post-reaction XPS spectra revealed surface structural changes in the catalyst after CO_2RR in different electrolytes. In the O1s core-level spectrum (Fig. S22), the peak corresponding to O_L retained comparable position and intensity after the reaction in both SO_4^{2-} and ClO_4^{-} electrolytes, but shifted by 0.8 eV (from 530.4 to 531.2 eV) in PO_4^{2-} electrolytes, indicating a decrease in electron density [88]. A similar trend was seen in the Bi 4 f spectrum, where the 4 $f_{5/2}$ and 4 $f_{7/2}$ orbitals upshifted 0.5 eV and 0.18 eV, respectively, for catalysts in H_3PO_4 and $HClO_4$ electrolytes. These results suggest that anions in the electrolyte affect the electron density of surface species, potentially altering the binding of key intermediates to the catalyst, and consequently, lead to variations in product distribution [89].

In situ FTIR measurements (Figs. 5c and 5d) further revealed that the variations in product distribution could be attributed to the distinct adsorption behaviors of anions on the dual metal oxide catalyst. For the spectra collected in phosphoric acid buffer, characteristic phosphate peaks at 1050 cm^{-1} and 1007 cm^{-1} [90], were not observed on the catalyst surface at OCP or low potentials. Conversely, an initial sulfate adsorption peak was detected in spectra collected in H_2SO_4. For ClO_4^{-} ions, the characteristic peak at 1157 cm^{-1} was observed at OCP, but with much lower peak intensity compared to the spectrum collected in H_2SO_4 electrolyte[91]. These observations align with prior studies identifying SO_4^{2-} as a strongly adsorbed anion and ClO_4^{-} has been long-term regarded as a nonspecifically adsorbed anion [92]. Additionally, SO_4^{2-} adsorption was noted on the polycrystalline Cu surface at the initial state of the catalyst surface while phosphate anions are reported to not adsorb at low potentials [93].

Such difference was found to influence the adsorption of molecules and atomic hydrogen production by alternating the active sites [94]. As evidence, we noted a peak located between 1800 and 1900 cm^{-1} in $HClO_4$ and H_3PO_4 electrolyte but absent for SO_4^{2-} electrolyte that represents the formation of bridged *CO. The bridged *CO adsorbate is

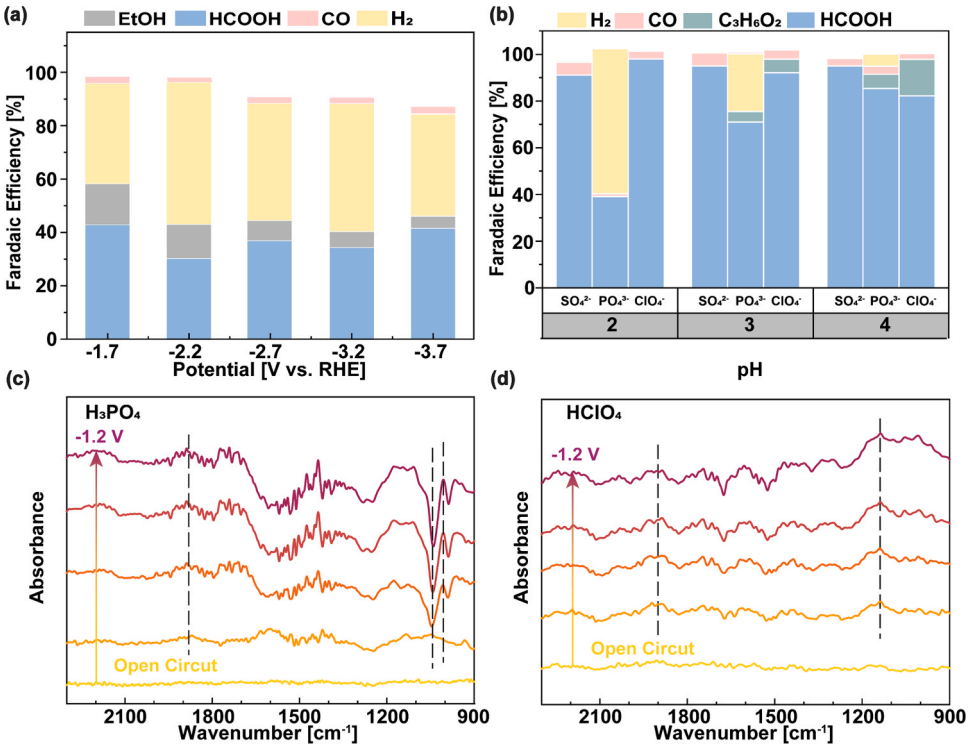

Fig. 5. (a, b) FE of CuO_x/BiO_x in CO_2 saturated (a) pH = 3, $[K^+]$ = 1.1 M phosphoric acid buffer and (b) $[K^+]$ = 0.5 M H_2SO_4, H_3PO_4, and $HClO_4$ electrolytes, tested at −2.2 V *vs.* RHE. *In situ* SR-FTIR of CuO_x/BiO_x in (c) H_3PO_4 and (d) $HClO_4$, from OCP to −1.2 V *vs.* RHE.

found to be prone to deep protonation into $*OCH_3$ intermediate, thus accelerating the coupling of *CO and $*OCH_3$ intermediates to generate C_{2+} alcohols [95–98]. Accordingly, we found that different anions exhibits distinct adsorption behaviors and consequently, leads to the formation of different intermediates and tuning product distributions. This offers a novel approach to enhancing C_{2+} product formation in electrochemical processes. However, we acknowledge that further systematic investigation is necessary to fully elucidate the effect of electrolyte composition. In particular, advanced in situ techniques and the incorporation of DFT calculations will be essential to gain a more comprehensive understanding of the underlying mechanisms by which electrolyte anions govern CO_2RR product selectivity.

4. Conclusion

In this study, we demonstrate the incorporation of BiO_x and CuO_x matrix to enhance the stability of the catalyst for acidic CO_2RR. At −2.7 V vs. RHE (-1.4 $V_{iR\text{-}compensated}$), the FE of HCOOH reached the highest of 97 ± 1.1 % and the yield of 476.3 nmol s^{-1} cm^{-2}. The catalyst also demonstrates excellent stability with FE of HCOOH maintained above 90 % for 20 h. *In situ* characterizations show that metastable BiO_x plays a crucial role in stabilizing site Cu_2O species, and the production of HCOOH is though the HCOO* pathway. Theoretical calculations indicate that the CuO_x/BiO_x catalyst inhibits *H adsorption, effectively suppressing the HER and increasing the free energy difference between *CO and *HCOOH, which promotes the selective conversion of CO_2 to formic acid. Additionally, our findings highlight that anion modulation in the electrolyte plays a critical role in controlling product selectivity and distribution. The catalyst achieves optimal formic acid selectivity in a sulfuric acid electrolyte, while ethanol and acetone are produced with Faradaic efficiencies of 16.8 % and 16.4 % in phosphoric acid buffer and perchloric acid electrolytes, respectively. *In situ* analyses revealed the distinct adsorption behavior of anions, resulting in the formation of bridged-adsorbed *CO intermediates, which facilitates the deep protonation into $*OCH_3$ intermediates and tune the selectivity towards C_{2+} products. This work provides valuable insights into the design of acid-stable electrocatalysts for efficient acidic CO_2RR and highlights the potential of tuning product selectivity through electrolyte modification.

CRediT authorship contribution statement

Ziling Zhang: Conceptualization, Investigation, Data curation, Writing – Original Draft, Writing – review & editing. **Thành Trần-Phú:** Methodology, Investigation, Formal analysis, Writing – Review & Editing. **Jodie Yuwono:** Software, Formal analysis, Data curation. **Zhipeng Ma:** Validation, Resources, Writing – Review & Editing. **Yuwei Yang:** Formal analysis. **Josh Leverett:** Writing – Review & Editing. **Rosalie K. Hocking:** Methodology, Investigation, Formal analysis, Writing – Review & Editing. **Bernt Johannesson:** Visualization, Validation, Software, Data curation. **Priyank Kumar:** Software, Formal analysis. **Rose Amal:** Writing – Review & Editing, Supervision, Resources, Funding acquisition. **Rahman Daiyan:** Conceptualization, Writing – Review & Editing, Supervision, Funding acquisition.

Declaration of Competing Interest

The authors declare that they have no known competing financial interests or personal relationships that could have appeared to influence the work reported in this paper.

Acknowledgements

The work was supported by the Australian Research Council (ARC) Training Centre for The Global Hydrogen Economy. A part of this research was undertaken in the characterization facility, including the surface analysis laboratory (SSEAU) and the spectroscopy laboratory (SPECLAB) within the Mark Wainwright Analytical Centre (MWAC) at the University of New South Wales. The authors also acknowledge the grant for synchrotron IR beamtime and XAS beamtime at the Australian Synchrotron and thank Dr. Jitraporn Vongsvivut and Shujie Zhou for

their supports and assistances with the *in situ* synchrotron (SR)-FTIR. R. D. acknowledges support from ARC Discovery Early Career Researcher Award (DECRA) DE230101396 and UNSW Scientia Fellowship.

Appendix A. Supporting information

Supplementary data associated with this article can be found in the online version at doi:10.1016/j.apcatb.2025.125203.

Data Availability

Data will be made available on request.

References

[1] C.E. Creissen, M. Fontecave, Solar-driven electrochemical CO2 reduction with heterogeneous catalysts, Adv. Energy Mater. 11 (2021) 2002652.
[2] B. Qiu, M. Du, Y. Ma, Q. Zhu, M. Xing, J. Zhang, Integration of redox cocatalysts for artificial photosynthesis, Energy Environ. Sci. 14 (2021) 5260–5288.
[3] V. Andrei, B. Reuillard, E. Reisner, Bias-free solar syngas production by integrating a molecular cobalt catalyst with perovskite–BiVO4 tandems, Nat. Mater. 19 (2020) 189–194.
[4] Y. Pang, T. Burdyny, C.-T. Dinh, M.G. Kibria, J.Z. Fan, M. Liu, E.H. Sargent, D. Sinton, Joint tuning of nanostructured Cu-oxide morphology and local electrolyte programs high-rate CO2 reduction to C2H4, Green. Chem. 19 (2017) 4023–4030.
[5] R. Kas, R. Kortlever, H. Yılmaz, M.T.M. Koper, G. Mul, Manipulating the hydrocarbon selectivity of copper nanoparticles in CO2 electroreduction by process conditions, ChemElectroChem 2 (2015) 354–358.
[6] J.-J. Lv, M. Jouny, W. Luc, W. Zhu, J.-J. Zhu, F. Jiao, A highly porous copper electrocatalyst for carbon dioxide reduction, Adv. Mater. 30 (2018) 1803111.
[7] M.G. Kibria, C.-T. Dinh, A. Seifitokaldani, P. De Luna, T. Burdyny, R. Quintero-Bermudez, M.B. Ross, O.S. Bushuyev, F.P. García de Arquer, P. Yang, D. Sinton, E. H. Sargent, A surface reconstruction route to high productivity and selectivity in CO2 electroreduction toward C2+ Hydrocarbons, Adv. Mater. 30 (2018) 1804867.
[8] T. Burdyny, W.A. Smith, CO2 reduction on gas-diffusion electrodes and why catalytic performance must be assessed at commercially-relevant conditions, Energy Environ. Sci. 12 (2019) 1442–1453.
[9] C.T. Dinh, T. Burdyny, M.G. Kibria, A. Seifitokaldani, C.M. Gabardo, F.P. García de Arquer, A. Kiani, J.P. Edwards, P. De Luna, O.S. Bushuyev, C. Zou, R. Quintero-Bermudez, Y. Pang, D. Sinton, E.H. Sargent, CO(2) electroreduction to ethylene via hydroxide-mediated copper catalysis at an abrupt interface, Science 360 (2018) 783–787.
[10] Z. Zhang, L. Melo, R.P. Jansonius, F. Habibzadeh, E.R. Grant, C.P. Berlinguette, pH Matters when reducing CO2 in an electrochemical flow cell, ACS Energy Lett. 5 (2020) 3101–3107.
[11] X. Liu, P. Schlexer, J. Xiao, Y. Ji, L. Wang, R.B. Sandberg, M. Tang, K.S. Brown, H. Peng, S. Ringe, C. Hahn, T.F. Jaramillo, J.K. Nørskov, K. Chan, pH Effects on the electrochemical reduction of CO((2)) towards C(2) products on stepped copper, Nat. Commun. 10 (2019) 32.
[12] M.C.O. Monteiro, F. Dattila, B. Hagedoorn, R. García-Muelas, N. López, M.T. M. Koper, Absence of CO2 electroreduction on copper, gold and silver electrodes without metal cations in solution, Nat. Catal. 4 (2021) 654–662.
[13] A.J. Welch, A.Q. Fenwick, A. Böhme, H.-Y. Chen, I. Sullivan, X. Li, J.S. DuChene, C. Xiang, H.A. Atwater, Operando local pH measurement within gas diffusion electrodes performing electrochemical carbon dioxide reduction, J. Phys. Chem. C 125 (2021) 20896–20904.
[14] N. Wang, R.K. Miao, G. Lee, A. Vomiero, D. Sinton, A.H. Ip, H. Liang, E.H. Sargent, Suppressing the liquid product crossover in electrochemical CO2 reduction 2 (2021) 12–16.
[15] M. Dunwell, X. Yang, B.P. Setzler, J. Anibal, Y. Yan, B. Xu, Examination of near-electrode concentration gradients and kinetic impacts on the electrochemical reduction of CO2 using surface-enhanced infrared spectroscopy, ACS Catal. 8 (2018) 3999–4008.
[16] J.A. Rabinowitz, M.W. Kanan, The future of low-temperature carbon dioxide electrolysis depends on solving one basic problem, Nat. Commun. 11 (2020) 5231.
[17] C. Chen, Y. Li, P. Yang, Address the “alkalinity problem” in CO2 electrolysis with catalyst design and translation, Joule 5 (2021) 737–742.
[18] J.E. Huang, F. Li, A. Ozden, A. Sedighian Rasouli, F.P. García de Arquer, S. Liu, S. Zhang, M. Luo, X. Wang, Y. Lum, Y. Xu, K. Bertens, R.K. Miao, C.-T. Dinh, D. Sinton, E.H. Sargent, CO2 electrolysis to multicarbon products in strong acid, Science 372 (2021) 1074–1078.
[19] J. Gu, S. Liu, W. Ni, W. Ren, S. Haussener, X.J.N.C. Hu, Modulating electric field distribution by alkali cations for CO2 electroreduction in strongly acidic medium 5 (2022) 268–276.
[20] A. Ozden, F.P. García de Arquer, J.E. Huang, J. Wicks, J. Sisler, R.K. Miao, C. P. O'Brien, G. Lee, X. Wang, A.H. Ip, E.H. Sargent, D. Sinton, Carbon-efficient carbon dioxide electrolysers, Nat. Sustain. 5 (2022) 563–573.
[21] Z. Lei, T. Wang, B. Zhao, W. Cai, Y. Liu, S. Jiao, Q. Li, R. Cao, M. Liu, Recent progress in electrocatalysts for acidic water oxidation, Adv. Energy Mater. 10 (2020) 2000478.
[22] L. Li, P. Wang, Q. Shao, X. Huang, Recent progress in advanced electrocatalyst design for acidic oxygen evolution reaction, Adv. Mater. 33 (2021) 2004243.
[23] W. Liu, P. Zhai, A. Li, B. Wei, K. Si, Y. Wei, X. Wang, G. Zhu, Q. Chen, X. Gu, R. Zhang, W. Zhou, Y. Gong, Electrochemical CO2 reduction to ethylene by ultrathin CuO nanoplate arrays, Nat. Commun. 13 (2022) 1877.
[24] R. Yang, M. Wu, D. Huang, Y. Yang, Y. Liu, L. Zhang, F. Lai, B. You, J. Fang, T. Liu, Y. Liu, T. Zhai, Which dominates industrial–current–density CO2-to-C2+ electroreduction: Cuδ+ or the microenvironment? Energy Environ. Sci. (2024).
[25] Z. Gu, H. Shen, Z. Chen, Y. Yang, C. Yang, Y. Ji, Y. Wang, C. Zhu, J. Liu, J.J.J. Li, Efficient electrocatalytic CO2 reduction to C2+ alcohols at defect-site-rich Cu surface 5 (2021) 429–440.
[26] N. Ling, J. Zhang, M. Wang, Z. Wang, Z. Mi, S. Bin Dolmanan, M. Zhang, B. Wang, W. Ru Leow, J. Zhang, Y. Lum, Acidic media impedes tandem catalysis reaction pathways in electrochemical CO2 reduction, Angew. Chem. Int. Ed. 62 (2023) e202308782.
[27] Y. Li, F. Cui, M.B. Ross, D. Kim, Y. Sun, P. Yang, Structure-sensitive CO2 electroreduction to hydrocarbons on ultrathin 5-fold twinned copper nanowires, Nano Lett. 17 (2017) 1312–1317.
[28] Y. Cao, Z. Chen, P. Li, A. Ozden, P. Ou, W. Ni, J. Abed, E. Shirzadi, J. Zhang, D.J.N. C. Sinton, Surface hydroxide promotes CO2 electrolysis to ethylene in acidic conditions, Nat. Commun. 14 (2023) 2387.
[29] X.M.C. Ta, T. Trần-Phú, T.K.A. Nguyen, M. Chatti, R. Daiyan, Engineering oxygen-evolving catalysts for acidic water electrolysis, Appl. Phys. Rev. 11 (2024) 021321.
[30] Y.-J. Tang, M.-R. Gao, C.-H. Liu, S.-L. Li, H.-L. Jiang, Y.-Q. Lan, M. Han, S.-H. Yu, Porous molybdenum-based hybrid catalysts for highly efficient hydrogen evolution, Angew. Chem. 127 (2015) 13120–13124.
[31] X. Fan, Z. Peng, R. Ye, H. Zhou, X. Guo, M3C (M: Fe, Co, Ni) nanocrystals encased in graphene nanoribbons: an active and stable bifunctional electrocatalyst for oxygen reduction and hydrogen evolution reactions, ACS Nano 9 (2015) 7407–7418.
[32] R. Chattot, T. Asset, P. Bordet, J. Drnec, L. Dubau, F. Maillard, Beyond strain and ligand effects: microstrain-induced enhancement of the oxygen reduction reaction kinetics on various PtNi/C nanostructures, ACS Catal. 7 (2017) 398–408.
[33] L. Wang, V.A. Saveleva, S. Zafeiratos, E.R. Savinova, P. Lettenmeier, P. Gazdzicki, A.S. Gago, K.A. Friedrich, Highly active anode electrocatalysts derived from electrochemical leaching of Ru from metallic Ir0.7Ru0.3 for proton exchange membrane electrolyzers, Nano Energy 34 (2017) 385–391.
[34] X. Dai, Z. Li, Y. Ma, M. Liu, K. Du, H. Su, H. Zhuo, L. Yu, H. Sun, X. Zhang, Metallic cobalt encapsulated in bamboo-like and nitrogen-rich carbonitride nanotubes for hydrogen evolution reaction, ACS Appl. Mater. Interfaces 8 (2016) 6439–6448.
[35] X. Yang, H. Li, A.-Y. Lu, S. Min, Z. Idriss, M.N. Hedhili, K.-W. Huang, H. Idriss, L.-J. Li, Highly acid-durable carbon coated Co3O4 nanoarrays as efficient oxygen evolution electrocatalysts, Nano Energy 25 (2016) 42–50.
[36] T. Tran-Phu, H. Chen, R. Daiyan, M. Chatti, B. Liu, R. Amal, Y. Liu, D. R. Macfarlane, A.N. Simonov, A. Tricoli, Nanoscale TiO2 coatings improve the stability of an earth-abundant cobalt oxide catalyst during acidic water oxidation, ACS Appl. Mater. Interfaces 14 (2022) 33130–33140.
[37] X.M.C. Ta, T. Trần-Phú, J.A. Yuwono, T.K.A. Nguyen, A.D. Bui, T.N. Truong, L.-c Chang, E. Magnano, R. Daiyan, A.N. Simonov, A. Tricoli, Optimal coatings of Co3O4 anodes for acidic water electrooxidation, Small 20 (2024) 2304650.
[38] X. Liu, J. Xiao, H. Peng, X. Hong, K. Chan, J.K. Nørskov, Understanding trends in electrochemical carbon dioxide reduction rates, Nat. Commun. 8 (2017) 15438.
[39] C. Zhu, L. Zhou, Z. Zhang, C. Yang, G. Shi, S. Zhao, H. Gu, J. Wu, X. Gao, Y. Li, K. Liu, S. Dai, L. Zhang, Dynamic restructuring of epitaxial Au–Cu biphasic interface for tandem CO2-to-C2+ alcohol conversion, Chem 8 (2022) 3288–3301.
[40] L. Li, Z. Liu, X. Yu, M. Zhong, Achieving high single-pass carbon conversion efficiencies in durable CO2 electroreduction in strong acids via electrode structure engineering, Angew. Chem. Int. Ed. 62 (2023) e202300226.
[41] Y. Zhao, L. Hao, A. Ozden, S. Liu, R.K. Miao, P. Ou, T. Alkayyali, S. Zhang, J. Ning, Y.J.N.S. Liang, Conversion of CO2 to multicarbon products in strong acid by controlling the catalyst microenvironment, Nat. Synth. (2023) 1–10.
[42] J. Zhang, C. Guo, S. Fang, X. Zhao, L. Li, H. Jiang, Z. Liu, Z. Fan, W. Xu, J. Xiao, M. Zhong, Accelerating electrochemical CO2 reduction to multi-carbon products via asymmetric intermediate binding at confined nanointerfaces, Nat. Commun. 14 (2023) 1298.
[43] Y. Xie, P. Ou, X. Wang, Z. Xu, Y.C. Li, Z. Wang, J.E. Huang, J. Wicks, C. McCallum, N.J.N.C. Wang, High carbon utilization in CO2 reduction to multi-carbon products in acidic media, Nat. Catal. 5 (2022) 564–570.
[44] X. Yu, Y. Xu, L. Li, M. Zhang, W. Qin, F. Che, M. Zhong, Coverage enhancement accelerates acidic CO2 electrolysis at ampere-level current with high energy and carbon efficiencies, Nat. Commun. 15 (2024) 1711.
[45] X. Zi, Y. Zhou, L. Zhu, Q. Chen, Y. Tan, X. Wang, M. Sayed, E. Pensa, R.A. Geioushy, K. Liu, J. Fu, E. Cortés, M. Liu, Breaking K^+ concentration limit on Cu nanoneedles for acidic electrocatalytic CO2 reduction to multi-carbon products, Angew. Chem. Int. Ed. 62 (2023) e202309351.
[46] Z. Ma, Z. Yang, W. Lai, Q. Wang, Y. Qiao, H. Tao, C. Lian, M. Liu, C. Ma, A.J.N. C. Pan, CO2 electroreduction to multicarbon products in strongly acidic electrolyte via synergistically modulating the local microenvironment, Nat. Commun. 13 (2022) 7596.
[47] N. Nie, D. Zhang, Z. Wang, S. Ge, Y. Gu, B. Yang, J. Lai, L. Wang, Stable p-block metals electronic perturbation in PtM@CNT (M=Ga, In, Pb and Bi) for acidic seawater hydrogen production at commercial current densities, Appl. Catal. B: Environ. 322 (2023) 122100.
[48] A.E. Thorarinsdottir, C. Costentin, S.S. Veroneau, D.G. Nocera, p-Block metal oxide noninnocence in the oxygen evolution reaction in acid: the case of bismuth oxide, Chem. Mater. 34 (2022) 826–835.

[49] T.A. Evans, K.-S. Choi, Electrochemical synthesis and investigation of stoichiometric, phase-pure CoSb2O6 and MnSb2O6 electrodes for the oxygen evolution reaction in acidic media, ACS Appl. Energy Mater. 3 (2020) 5563–5571.
[50] T. Tran-Phu, R. Daiyan, X.M.C. Ta, R. Amal, A. Tricoli, Tricoli, from stochastic self-assembly of nanoparticles to nanostructured (photo)electrocatalysts for renewable power-to-X applications via scalable flame synthesis, Adv. Funct. Mater. 32 (2022) 2110020.
[51] T. Tran-Phu, R. Daiyan, Z. Fusco, Z. Ma, R. Amal, A. Tricoli, Nanostructured β-Bi2O3, Nanostructured β-Bi2O3 fractals on carbon fibers for highly selective CO2 electroreduction to formate, Adv. Funct. Mater. 30 (2020) 1906478.
[52] T. Tran-Phu, M. Chatti, J. Leverett, T.K.A. Nguyen, D. Simondson, D.A. Hoogeveen, A. Kiy, T. Duong, B. Johannessen, J. Meilak, P. Kluth, R. Amal, A.N. Simonov, R. K. Hocking, R. Daiyan, A. Tricoli, Understanding the role of (W, Mo, Sb) dopants in the catalyst evolution and activity enhancement of Co3O4 during water electrolysis via in situ spectroelectrochemical techniques, Small 19 (2023) 2208074.
[53] T. Tran-Phu, R. Daiyan, Z. Fusco, Z. Ma, L.R.A. Rahim, A. Kiy, P. Kluth, X. Guo, Y. Zhu, H. Chen, R. Amal, A. Tricoli, Multifunctional nanostructures of Au–Bi2O3 fractals for CO2 reduction and optical sensing, J. Mater. Chem. A 8 (2020) 11233–11245.
[54] R.D. Deslattes, E.G.K. Jr, P. Indelicato, Ld Billy, E. Lindroth, J. Anton, J.S. Coursey, D.J. Schwab, J. Chang, R. Sukumar, K. Olsen, R.A. Dragoset, X-Ray Transition Energies Database, NIST, Physical Measurement Laboratory, 2005.
[55] B. Ravel, M. Newville, Athena, Artemis, Hephaestus: data analysis for X-ray absorption spectroscopy using IFEFFIT, J. Synchrotron Radiat. 12 (2005) 537–541.
[56] T. Tran-Phu, R. Daiyan, X.M.C. Ta, R. Amal, A. Tricoli, From stochastic self-assembly of nanoparticles to nanostructured (Photo) electrocatalysts for renewable power-to-X applications via scalable flame synthesis, Adv. Funct. Mater. 32 (2022) 2110020.
[57] N. Habbache, N. Alane, S. Djerad, L. Tifouti, Leaching of copper oxide with different acid solutions, Chem. Eng. J. 152 (2009) 503–508.
[58] S. Popović, M. Smiljanić, P. Jovanovič, J. Vavra, R. Buonsanti, N. Hodnik, Stability and degradation mechanisms of copper-based catalysts for electrochemical CO2 reduction, Angew. Chem. Int. Ed. 59 (2020) 14736–14746.
[59] M. Yang, X. Zhao, L. Ma, Y. Yao, Y. Ding, X. Shen, Electrochemical properties of Cu2O/Cu composite particles prepared by a novel and facile method, Electrochim. Acta 56 (2011) 5783–5787.
[60] E. Arulkumar, S. Thanikaikarasan, N. Tesfie, Influence of deposition parameters for Cu2O and CuO thin films by electrodeposition technique: a short review, J. Nanomater. 2023 (2023) 8987633.
[61] X. Wang, M. Luo, J. Lan, M. Peng, Y. Tan, Nanoporous intermetallic Pd3Bi for efficient electrochemical nitrogen reduction, Adv. Mater. 33 (2021) 2007733.
[62] Z. Jiang, S. Ren, X. Cao, Q. Fan, R. Yu, J. Yang, J. Mao, pH-Universal electrocatalytic CO2 reduction with ampere-level current density on doping-engineered bismuth sulfide, Angew. Chem. Int. Ed. 63 (2024) e202408412.
[63] Z. Ma, T. Wan, D. Zhang, J.A. Yuwono, C. Tsounis, J. Jiang, Y.-H. Chou, X. Lu, P. V. Kumar, Y.H. Ng, D. Chu, C.Y. Toe, Z. Han, R. Amal, Atomically dispersed Cu catalysts on sulfide-derived defective ag nanowires for electrochemical CO2 reduction, ACS Nano 17 (2023) 2387–2398.
[64] K. Chen, Z. Ma, X. Li, J. Kang, D. Ma, K. Chu, Single-atom Bi alloyed pd metallene for nitrate electroreduction to ammonia, Adv. Funct. Mater. 33 (2023) 2209890.
[65] W. Zhang, S. Zhan, J. Xiao, T. Petit, C. Schlesiger, M. Mellin, J.P. Hofmann, T. Heil, R. Müller, K. Leopold, M. Oschatz, Coordinative stabilization of single bismuth sites in a carbon–nitrogen matrix to generate atom-efficient catalysts for electrochemical nitrate reduction to ammonia, Adv. Sci. 10 (2023) 2302623.
[66] S. Luke, M. Chatti, D. Simondson, K.N. Dinh, B.V. Kerr, T.D. Nguyen, G. Yilmaz, B. Johannessen, D.R. MacFarlane, A. Yella, R.K. Hocking, A.N. Simonov, High performance acidic water electrooxidation catalysed by manganese–antimony oxides promoted by secondary metals, EES Catal. 1 (2023) 730–741.
[67] N.J.GsoJofr Takeno, Atlas Eh-pH Diagr. 419 (2005) 285.
[68] X.-D. Liang, Q.-Z. Zheng, N. Wei, Y.-Y. Lou, S.-N. Hu, K.-M. Zhao, H.-G. Liao, N. Tian, Z.-Y. Zhou, S.-G. Sun, In-situ constructing Bi@Bi2O2CO3 nanosheet catalyst for ampere-level CO2 electroreduction to formate, Nano Energy 114 (2023) 108638.
[69] H. Shen, Y. Zhao, L. Zhang, Y. He, S. Yang, T. Wang, Y. Cao, Y. Guo, Q. Zhang, H. Zhang, In-situ constructuring of copper-doped bismuth catalyst for highly efficient CO2 electrolysis to formate in ampere-level, Adv. Energy Mater. 13 (2023) 2202818.
[70] W. Oh, C.K. Rhee, J.W. Han, B. Shong, Atomic and molecular adsorption on the Bi (111) surface: insights into catalytic CO2 reduction, J. Phys. Chem. C 122 (2018) 23084–23090.
[71] S. Trasatti, Work function, electronegativity, and electrochemical behaviour of metals: III. Electrolytic hydrogen evolution in acid solutions, J. Electroanal. Chem. Interfacial Electrochem. 39 (1972) 163–184.
[72] J. Choi, H.-L. Du, M. Chatti, B.H.R. Suryanto, A.N. Simonov, D.R. MacFarlane, Reassessment of the catalytic activity of bismuth for aqueous nitrogen electroreduction, Nat. Catal. 5 (2022) 382–384.
[73] C. Cao, D.-D. Ma, J.-F. Gu, X. Xie, G. Zeng, X. Li, S.-G. Han, Q.-L. Zhu, X.-T. Wu, Q. Xu, Metal–organic layers leading to atomically thin bismuthene for efficient carbon dioxide electroreduction to liquid fuel, Angew. Chem. Int. Ed. 59 (2020) 15014–15020.
[74] X. Zhang, X. Sun, S.-X. Guo, A.M. Bond, J.J.E. Zhang, E. Science, Formation of lattice-dislocated bismuth nanowires on copper foam for enhanced electrocatalytic CO 2 reduction at low overpotential, Energy Environ. Sci. 12 (2019) 1334–1340.
[75] S. Nitopi, E. Bertheussen, S.B. Scott, X. Liu, A.K. Engstfeld, S. Horch, B. Seger, I.E. L. Stephens, K. Chan, C. Hahn, J.K. Nørskov, T.F. Jaramillo, I. Chorkendorff, Progress and perspectives of electrochemical CO2 reduction on copper in aqueous electrolyte, Chem. Rev. 119 (2019) 7610–7672.
[76] C.W. Li, M.W. Kanan, CO2 Reduction at low overpotential on Cu electrodes resulting from the reduction of thick Cu2O films, J. Am. Chem. Soc. 134 (2012) 7231–7234.
[77] F.M. Toma, J.K. Cooper, V. Kunzelmann, M.T. McDowell, J. Yu, D.M. Larson, N. J. Borys, C. Abelyan, J.W. Beeman, K.M. Yu, J. Yang, L. Chen, M.R. Shaner, J. Spurgeon, F.A. Houle, K.A. Persson, I.D. Sharp, Mechanistic insights into chemical and photochemical transformations of bismuth vanadate photoanodes, Nat. Commun. 7 (2016) 12012.
[78] Z. Wu, H. Wu, W. Cai, Z. Wen, B. Jia, L. Wang, W. Jin, T. Ma, Engineering Bismuth–Tin interface in bimetallic aerogel with a 3D porous structure for highly selective electrocatalytic CO2 reduction to HCOOH, Angew. Chem. Int. Ed. 60 (2021) 12554–12559.
[79] Park, R.B. Gupta, C.W. Curtis, C.B. Roberts, Solvent effects on the self-association of formic acid in carbon dioxide and ethane, J. Phys. Chem. B 106 (2002) 9696–9700.
[80] M. Zhao, Y. Gu, W. Gao, P. Cui, H. Tang, X. Wei, H. Zhu, G. Li, S. Yan, X. Zhang, Z. Zou, Atom vacancies induced electron-rich surface of ultrathin Bi nanosheet for efficient electrochemical CO2 reduction, Appl. Catal. B: Environ. 266 (2020) 118625.
[81] W. Ma, S. Xie, T. Liu, Q. Fan, J. Ye, F. Sun, Z. Jiang, Q. Zhang, J. Cheng, Y. Wang, Electrocatalytic reduction of CO2 to ethylene and ethanol through hydrogen-assisted C–C coupling over fluorine-modified copper, Nat. Catal. 3 (2020) 478–487.
[82] M. Futamata, L. Luo, C. Nishihara, ATR–SEIR study of anions and water adsorbed on platinum electrode, Surf. Sci. 590 (2005) 196–211.
[83] J.T. Feaster, C. Shi, E.R. Cave, T. Hatsukade, D.N. Abram, K.P. Kuhl, C. Hahn, J. K. Nørskov, T.F. Jaramillo, Understanding selectivity for the electrochemical reduction of carbon dioxide to formic acid and carbon monoxide on metal electrodes, ACS Catal. 7 (2017) 4822–4827.
[84] Z. Li, B. Sun, D. Xiao, Z. Wang, Y. Liu, Z. Zheng, P. Wang, Y. Dai, H. Cheng, B. Huang, Electron-Rich Bi nanosheets promote CO2·− formation for high-performance and pH-universal electrocatalytic CO2 reduction, Angew. Chem. Int. Ed. 62 (2023) e202217569.
[85] J. Resasco, Y. Lum, E. Clark, J.Z. Zeledon, A.T. Bell, Effects of anion identity and concentration on electrochemical reduction of CO2, ChemElectroChem 5 (2018) 1064–1072.
[86] P. Sebastián-Pascual, A.S. Petersen, A. Bagger, J. Rossmeisl, M. Escudero-Escribano, pH and anion effects on Cu–phosphate interfaces for CO electroreduction, ACS Catal. 11 (2021) 1128–1135.
[87] C.J. Bondue, M. Graf, A. Goyal, M.T.M. Koper, Suppression of hydrogen evolution in acidic electrolytes by electrochemical CO2 reduction, J. Am. Chem. Soc. 143 (2020) 279–285.
[88] J.F. Moulder, S.F. Stickle, P.E. Sobol, K.D. Bomben. Handbook of X-ray photoelectron spectroscopy, Perkin-Elmer Corporation, 1992.
[89] Y. Katayama, F. Nattino, L. Giordano, J. Hwang, R.R. Rao, O. Andreussi, N. Marzari, Y. Shao-Horn, An in situ surface-enhanced infrared absorption spectroscopy study of electrochemical CO2 reduction: selectivity dependence on surface C-bound and O-bound reaction intermediates, J. Phys. Chem. C 123 (2019) 5951–5963.
[90] D. Luna-Zaragoza, E.T. Romero-Guzmán, L.R. Reyes-Gutiérrez, Surface and physicochemical characterization of phosphates vivianite, Fe2(PO4)3 and hydroxyapatite, ca5(PO4)3OH, J. Miner. Mater. Charact. Eng. 08 (2009) 591–609.
[91] Y. Sawatari, J. Inukai, M. Ito, The structure of bisulfate and perchlorate on a Pt (111) electrode surface studied by infrared spectroscopy and ab-initio molecular orbital calculation, J. Electron Spectrosc. Relat. Phenom. 64 (65) (1993) 515–522.
[92] S. Zhu, X. Hu, L. Zhang, M. Shao, Impacts of perchloric acid, nafion, and alkali metal ions on oxygen reduction reaction kinetics in acidic and alkaline solutions, J. Phys. Chem. C. 120 (2016) 27452–27461.
[93] C. Schlaup, S. Horch, In-situ STM study of phosphate adsorption on Cu(111), Au (111) and Cu/Au(111) electrodes, Surf. Sci. 608 (2013) 44–54.
[94] P. Dubé, G.M. Brisard, Influence of adsorption processes on the CO2 electroreduction: An electrochemical mass spectrometry study, J. Electroanal. Chem. 582 (2005) 230–240.
[95] J. Salimon, R.M. Hernández-Romero, M. Kalaji, The dynamics of the conversion of linear to bridge bonded CO on Cu, J. Electroanal. Chem. 538-539 (2002) 99–108.
[96] S.K. Shaw, A. Berná, J.M. Feliu, R.J. Nichols, T. Jacob, D.J. Schiffrin, Role of axially coordinated surface sites for electrochemically controlled carbon monoxide adsorption on single crystal copper electrodes, Phys. Chem. Chem. Phys. 13 (2011) 5242–5251.
[97] C.M. Gunathunge, V.J. Ovalle, Y. Li, M.J. Janik, M.M. Waegele, Existence of an electrochemically inert CO population on Cu electrodes in alkaline pH, ACS Catal. 8 (2018) 7507–7516.
[98] Z. Li, B. Sun, D. Xiao, H. Liu, Z. Wang, Y. Liu, Z. Zheng, P. Wang, Y. Dai, B. Huang, H. Cheng, Mesostructure-specific configuration of *CO adsorption for selective CO2 electroreduction to C2+ products, Angew. Chem. (2024) e202413832.